SCIENTIFIC REPORTS
nature research

OPEN

# Structural, Magnetic, and Dielectric properties of $Sr_4Fe_6O_{13}$ ferrite prepared of small crystallites

A. A. Azab[1*], A. M. Mansour[1] & G. M. Turky[2]

**A stable $Sr_4Fe_6O_{13}$ was prepared as small crystallites by auto-combustion of a sol-gel in air followed by annealing the later at pertinent temperatures. A green sample, as annealed at elevated temperatures, yields a single $Sr_4Fe_6O_{13}$ phase of tailored magnetic properties. The structural, morphological, magnetic and electrical properties were investigated by X-ray diffraction, transmission electron microscopy, vibrating sample magnetometer, and broadband dielectric spectrometer. Hard magnetic $Sr_4Fe_6O_{13}$ properties arise with saturation magnetization $M_s = 12.4$ emu/g, coercivity $H_c = 3956.7$ Oe and squareness 0.512. Studies made at low temperatures reveals $M_s$ decreasing on increasing temperature from 17.5 emu/g at 85 K down to 12.4 emu/g at 305 K, while $H_c$ rises from 1483 Oe at 85 K to 1944 Oe at 305 K. The ac-conductivity follows the Jonscher relation. The dc-conductivity at high temperatures/low frequencies exhibits a plateau and it depends linearly on a characteristic frequency according to the Barton-Nakajima-Namikawa) relation.**

Perovskites are compounds of a structural formula $ABC_3$, where A represents a rare earth, alkaline earth, alkali or large ions such as $Pb^{2+}$, $Bi^{3+}$, B represents a transition metal ion and C represents O, Fl, Cl, I etc[1]. A cation may be monovalent like Li, Na, K, divalent like Ca, Ba, Sr or trivalent like La, Nd, Pr, which is cubo-octahedrally coordinated to 12 $O^{2-}$ ions, while B cation, such as Ti, Ni, Fe, Co, or Mn is octahedrally coordinated to 6 $O^{2-}$ ions[2]. Recently, several investigations performed on a Sr-Fe-O structure reveal its amazing structural and physical features such as cheap price, high magnetic anisotropy, high Curie temperature, a significant magnetization of saturation and remarkable chemical and corrosion resistance[3]. The reason certainly presented by oxygen-lacking perovskites and by Ruddlesden-Popper (RP) type structure that possess a desirably negative magnetoresistance (-ve MR)[4–7]. A Sr-Fe-O system includes many types of perovskites and perovskite derivatives of widely varied crystalline and magnetic features[8–12]. These types of substances are constructed based on a $K_2NiF_4$ shape and involve slab segments of $SrFeO_3$ and SrO, where $SrFeO_3$ is resulting from a $KNiF_3$ cubic perovskite of $K_2NiF_4$, and SrO is matching to a NaCl-class KF[8]. They characteristically contain paramagnetic $Fe^{4+}$ ions.

In particular, a stoichiometric compound $Sr_4Fe_6O_{13}$ has a construction of a perovskite or its derivatives[8]. It is observed that a $Sr_4Fe_6O_{13\pm\delta}$ construction is a highly stable single-phase compound and it exhibits significant conductivity of combined-ions and electrons types[13]. That is composed of altered sections through a Sr-Fe-O layer (b-axis) and dual slabs of FeO in $FeO_5$ polygons[14–16]. As a result, it owes an anisotropic shape in it conducts through $O^{2-}$ ions and vacancies across the a-c planes[17]. Actually, creation of $O^{2-}$ empty sites and interstitials develop non-perovskite slabs in a $Sr_4Fe_6O_{13\pm\delta}$ phase keeps them in a broad array of $O^{2-}$ non-stoichiometry[18]. Mixed oxygen-ions and electron conducting oxides have attracted great interest owing to their promising use in ceramic separation filters of hydrocarbons incomplete oxidation and oxygen, fuel cell cathodes, or gas detectors[19–22].

According to the authors' best knowledge and after searching international scientific databases, there are a few studies done on a $Sr_4Fe_6O_{13}$ system. Little attention has been paid on its magnetic and electrical properties, whereas most studies are focused on its applications in oxygen membranes[23,24]. An auto-combustion method we used in the present work to prepare a stable $Sr_4Fe_6O_{13}$ of small crystallites. The as-prepared powder was annealed at different temperatures in order to get a single $Sr_4Fe_6O_{13}$ phase. A major objective of this work is to explore magnetic properties in small $Sr_4Fe_6O_{13}$ crystallites at and below room temperatures. Further, ac conductivity and dielectric properties are studied on a broad range of frequencies and at different temperatures.

[1]Solid State Electronics Laboratory, Solid State Physics Department, Physical Research Division, National Research Centre, 33 El-Bohouth St., Dokki, Giza, P.O. 12622, Egypt. [2]Microwave Physics & Dielectrics Department, Physical Research Division, National Research Centre, 33 El Bohouth St., Dokki, Giza, P.O. 12622, Egypt. *email: aliazab@hotmail.com

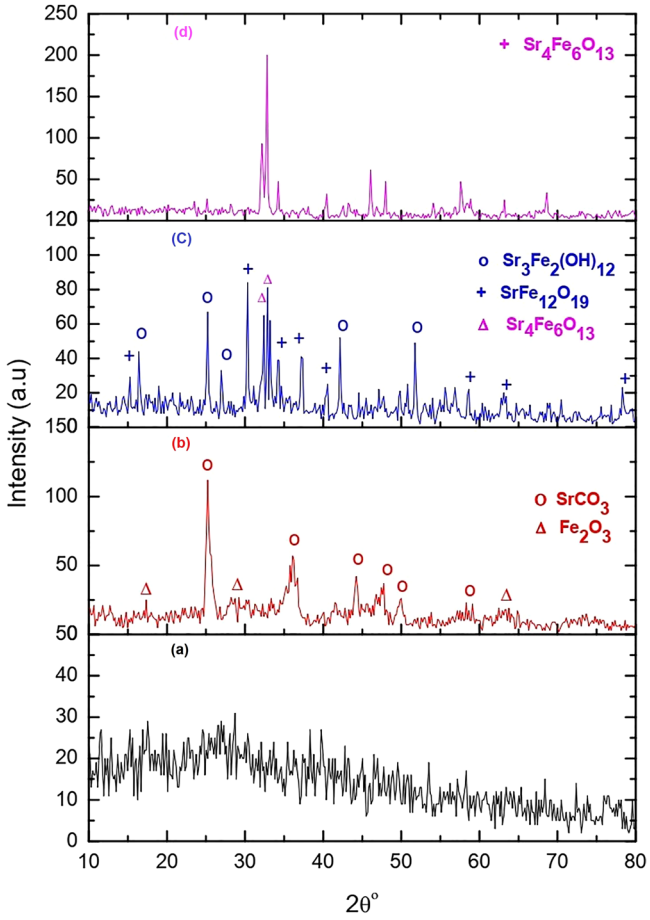


**Figure 1.** XRD patterns of (**a**) as-prepared ($S_0$) and annealed samples at (**b**) 500 °C for 3 h ($S_1$), (**c**) 1100 °C for 3 h ($S_2$), and (**d**) 1100 °C for 10 h ($S_3$).

## Results and discussion

**Structural properties.** X-ray diffraction (XRD) patterns of the various samples are shown in Fig. 1. The as-prepared sample $S_0$ in Fig. 1a reveals an amorphous pattern with no defined peaks. Figure 1b shows formation of two different phases in the as-prepared sample annealed at 500 °C for 3 h ($S_1$). The main phase of an orthorhombic $SrCO_3$ accompanies a secondary phase of a rhombohedral $\alpha$-$Fe_2O_3$ according to JCPDS files 00-005-0418 and 00-073-0603, respectively. The $SrCO_3$ forms in a chemical reaction of $Sr(NO_3)$ with $CO_2$ during the synthesis[25]. The diffraction pattern in Fig. 1c of sample $S_2$ annealed at 1100 °C for 3 h demonstrates three phases. The main phase orthorhombic $Sr_4Fe_6O_{13}$ contains two secondary phases of hexagonal $SrFe_{12}O_{19}$ and cubic $Sr_3Fe_2(OH)_{12}$. Figure 1d shows XRD of a single phase orthorhombic $Sr_4Fe_6O_{13}$ (according to JCPDS file 78-2403) of sample $S_3$ annealed at 1100 °C for 10 h. No any secondary phase is observed here. An average crystallite size of the fabricated powder was determined using the Scherrer relation[26,27].

$$D = k\lambda/\beta \cos\theta \tag{1}$$

Here, k is the shape factor (commonly taken approximately as 0.89), $\lambda$ is wavelength of the X-ray beam used, $\beta$ is the full-width at half maximum of (251) peak and $\theta$ is the diffraction angle. An average D-value of $Sr_4Fe_6O_{13}$ was found to be ~72 nm. A microstrain ($\alpha$) present in the $Sr_4Fe_6O_{13}$ crystallites was computed as per a model relation[26,27],

$$\alpha = \beta \cos\theta/4 \tag{2}$$

A typical $\alpha = 0.04$ value is found for sample $S_3$. A dislocation density $\delta = 1.92 \times 10^{17}$ lines/cm$^2$ (looked as a dislocation line length) contained therein is estimated as[28],

$$\delta = \frac{1}{D^2} \tag{3}$$

A scanning electron microscope (SEM) was used to examine morphology of the $Sr_4Fe_6O_{13}$ samples as illustrated in Fig. 2. Small grains are observed of irregular rectangular or cubic shapes, with an average size of 85 nm ($S_3$) in a good agreement with the D-value estimated from Scherrer relation. The $Sr_4Fe_6O_{13}$ images were studied

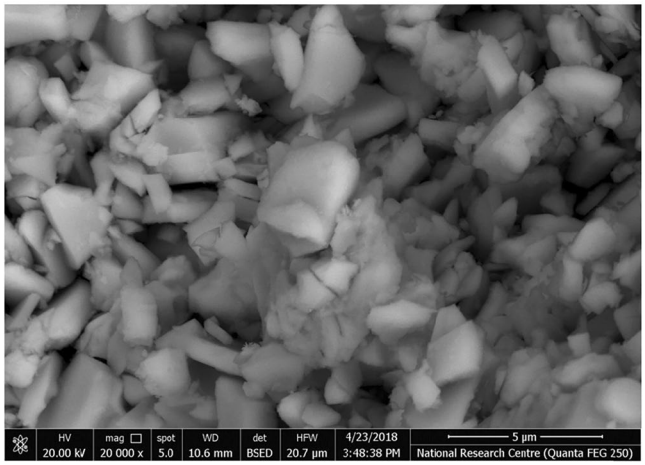


**Figure 2.** SEM images of sample $S_3$.

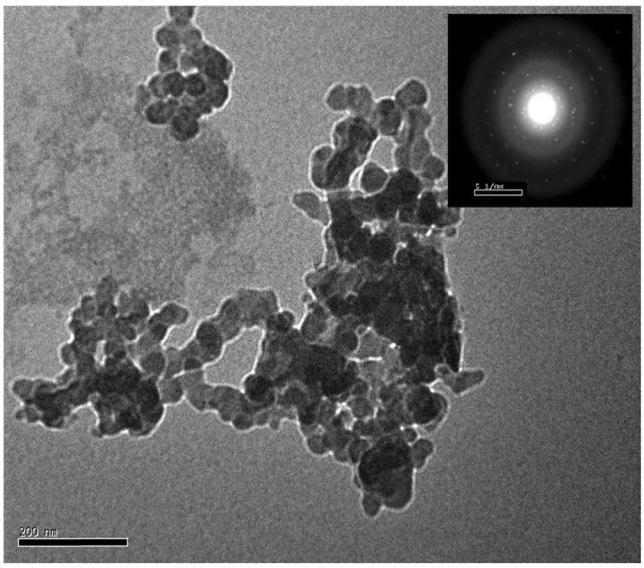


**Figure 3.** TEM images of sample $S_3$, with SAED pattern in the inset.

more closely in a transmission electron microscope (TEM) as given in Fig. 3. Small particles are observed with an average 68 nm size, which exhibit electron diffraction rings with spots, characterizing a nanocrystalline phase in agreement with the XRD analysis.

**Magnetic properties.** Figure 4 depicts magnetic hysteresis loops of samples $S_1$, $S_2$, and $S_3$ of a ferromagnetic behavior. Values of saturation magnetization ($M_s$), remanence magnetization ($M_r$), coercivity ($H_c$) and squareness ratio ($R = M_r/M_s$) determined from the loops are given in Table 1. Sample $S_1$ shows soft ferromagnetic behavior with $M_s = 5.8$ emu/g and $H_c = 102.0$ Oe. The main phase in this sample is $SrCO_3$, which has no magnetic moment. A secondary phase $Fe_2O_3$ contributes the magnetic features. Sample $S_2$ displays improved $M_s = 22.2$ emu/g, $H_c = 4223.6$ Oe, and $R = 0.487$ values as it contains a main phase $Sr_4Fe_6O_{13}$ with secondary phases $Sr_3Fe_2(OH)_{12}$ and $SrFe_{12}O_{19}$. The hexagonal ferrite $SrFe_{12}O_{19}$ is considered to be made up of alternating spinel ($S = Fe_6O_8^{2+}$) and hexagonal ($R = SrFe_6O_{11}^{2-}$) layers. The $O^{2-}$ ions are closely packed with $Sr^{2+}$ ions in a hexagonal layer and the $Fe^{3+}$ ions distribute in five distinct sites: three octahedral sites (12k, 2a and 4f2), one tetrahedral (4f1) site and one bipyramidal site (2b)[29]. The magnetic structure given by the Gorter model is ferromagnetic with five different sublattices, three parallel (12k, 2a, and 2b) and two anti-parallel (4f1 and 4f2), which are coupled with superexchange interactions through $O^{2-}$ ions[30]. The $Sr^{2+}$ ions are responsible for a large uniaxial magnetic anisotropy controls perturbation of the crystal lattice[31]. Zhang *et al.* demonstrated the $Sr_3Fe_2(OH)_{12}$ exhibits a weak ferromagnetic behavior with $M_s = 0.86$ emu/g and $H_c = 258.43$ Oe[32]. So, the magnetic behavior in sample $S_2$ is mainly due to the $SrFe_{12}O_{19}$ and $Sr_4Fe_6O_{13}$ ferrites. Further, sample $S_3$ has $M_s = 15.7$ emu/ g, $H_c = 3956.7$ G and $R = 0.512$ as measured at room temperature.

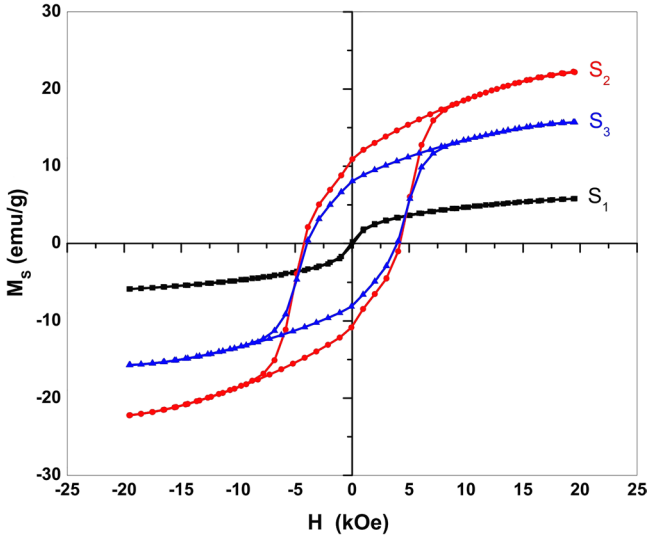


**Figure 4.** M-H Hysteresis loops for $S_1$, $S_2$, and $S_3$ samples.

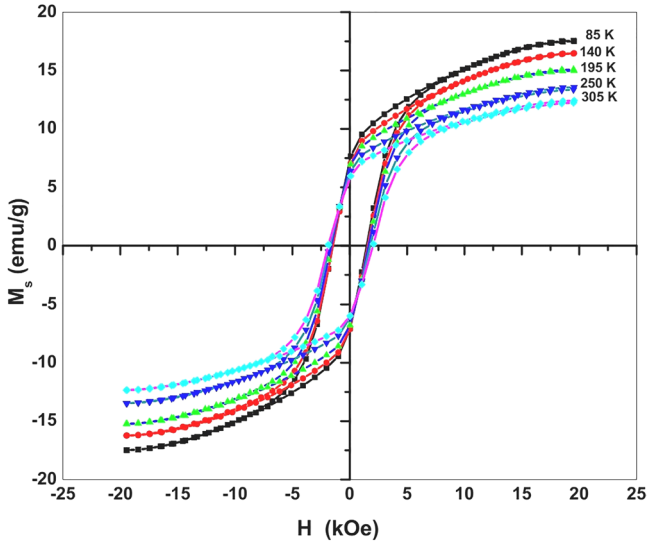


**Figure 5.** M-H hysteresis loops measured for sample $S_3$ at selected temperatures in a range of 85–305 K.

| Sample | $M_s$ (emu/g) | $M_r$ (emu/g) | $H_c$ (Oe) | R |
|---|---|---|---|---|
| $S_1$ | 5.8 | 0.2 | 102 | 0.03[4] |
| $S_2$ | 22.2 | 10.8 | 4223 | 0.48 |
| $S_3$ | 15.7 | 8.05[1] | 3956 | 0.51 |

**Table 1.** Magnetic properties of $Sr_4Fe_6O_{13}$ samples prepared in different conditions.

Figure 5 shows hysteresis loops of sample $S_3$ measured at different temperatures 85 to 305 K. As shown in Fig. 6a, the $M_s$ decreases with increasing temperature, assuming $M_s = 17.5$ emu/g at 85 K relative to $M_s = 12.4$ emu/g at 305 K. This is a typical behavior of ferromagnetic materials in the moment decreases on increasing thermal energy[33,34]. This can be realized by fitting the data using the Bloch's law[35–37].

$$M_s(T) = M_s(0)(1 - BT^{\alpha}) \tag{4}$$

where B is the Bloch constant and $M_s(0)$ is the $M_s$ at 0 K. A value $\alpha = 3/2$ is assigned according to the mean-field theory for long-range ferromagnetism, with $B = 10^{-4}$–$10^{-5}$ for nanoferrites and $10^{-6}$ for bulk ferromagnets. The

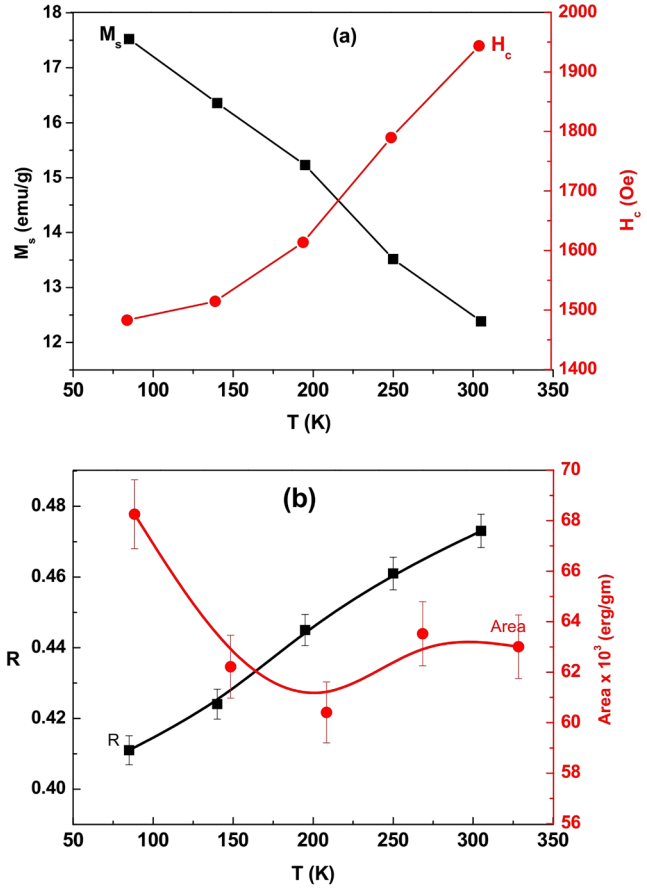


**Figure 6.** Variations of (**a**) $M_s$ and $H_c$ and (**b**) squareness (R) and hysteresis area measured against temperature for sample $S_3$.

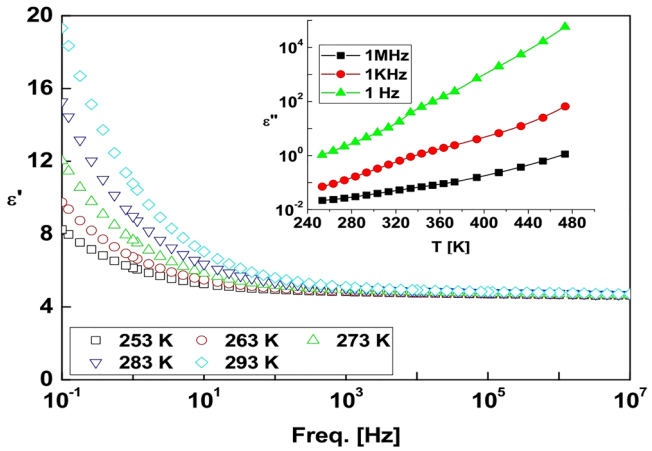


**Figure 7.** Frequency dependence of ε′-values measured for sample $S_0$ at selected temperatures in a range 253–293 K, with temperature ε′′dependence given in the inset at 1 Hz, 1 kHz, and 1 MHz frequencies.

Bloch's law is valid in our samples[36,38]. Cojocaru studied temperature $M_s$ dependence for ferromagnetic nanoparticles in the experimental data follow the Bloch's law[39]. Figure 6a also shows how $H_c$ growing with temperature from 1483 Oe at 85 K to 1944 Oe at 305 K. It is a complicated function of reversal mechanism of spins, anisotropy energy, and magnetic microstructure, viz., shape and size of crystallites, grain boundaries, surfaces, etc. There are also examples in it increasing with temperature[40–42]. Figure 6b shows how R peaks-up with temperature, while the area enclosed in a hysteresis loop decreases up to 195 K and then increases. The area enclosed in a hysteresis cycle represents an irreversible work required to go through the cycle. It depends on dissipation of energy in spin reversals over the fields.

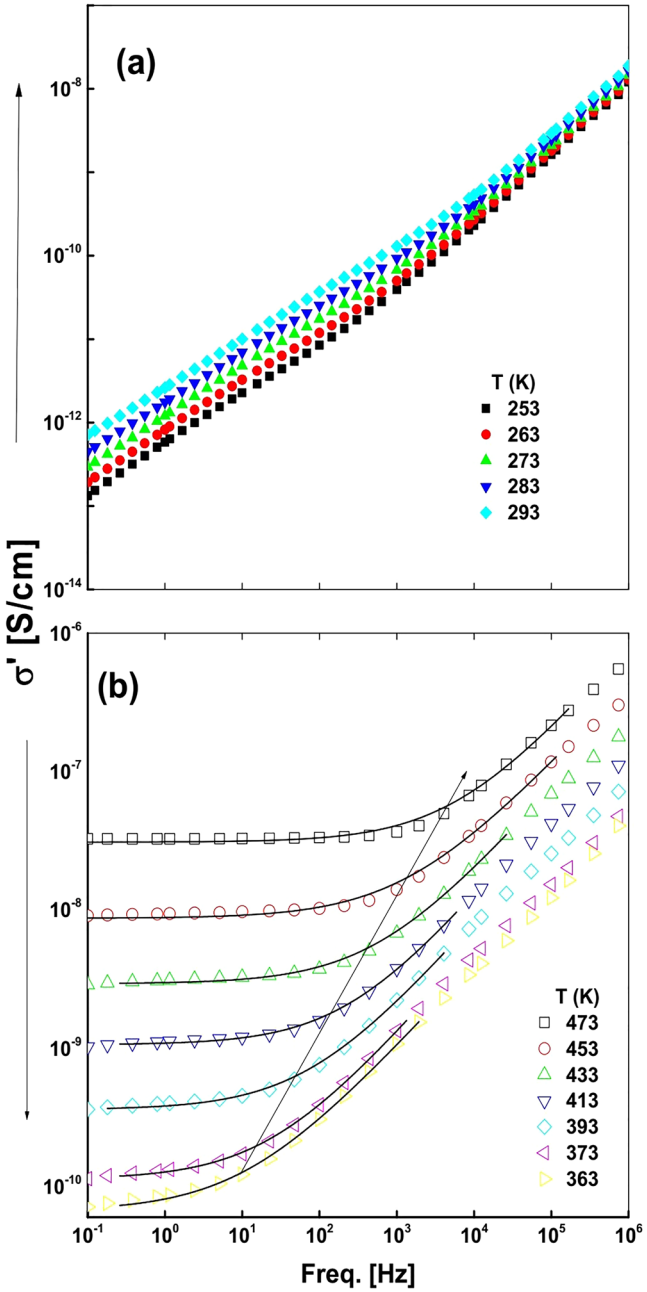


**Figure 8.** Frequency dependence of σ′-values measured for sample $S_0$ at selective temperatures in (**a**) 253–293 K and (**b**) 363–473 K regions.

**Dielectric and electrical properties.** Dielectric permittivity $\varepsilon'$ of sample $S_0$ varies in two different trends as plotted against frequency in Fig. 7 at different temperatures of 253 to 293 K. In the first region at frequencies above 1 kHz, no remarkable effect of frequency or temperature is noticed. In the second region below 1 kHz up to 0.1 Hz (limited according to the frequency window studied), the $\varepsilon'$ value rises progressively at lower frequencies. As usual[43,44], the temperature progressively promotes the final $\varepsilon'$ values. Two factors govern enhanced $\varepsilon'$ values at low frequencies; (i) space charge polarization and (ii) interfacial polarization due to domain-wall motion, usually found in multicomponent materials[45–47]. They have induced oscillations compatible to low frequencies of applied external electric fields that facilitate the $\varepsilon'$ values. A field induced charge transport favors conductivity and in turn density and mobility of active charge carriers. It also promotes the interfacial polarization observed here. As oscillations of the charge carriers are reasonably damped, the $\varepsilon'$ value is reduced at higher frequencies. In order to gain a more insight of the effect of temperature on the charge transport even at high frequencies, one has to study separately the effect of temperature on imaginary counter part $\varepsilon''$ of permittivity. The inset in Fig. 7 describes temperature $\varepsilon''$ dependence studied at $10^0$, $10^3$ and $10^6$ Hz frequencies. A resultant value $\varepsilon^*(\omega,T) = \varepsilon'(\omega,T) - i\varepsilon''(\omega,T)$ is related to the complex conductivity $\sigma^*(\omega,T) = \sigma'(\omega,T) + i\sigma''(\omega,T)$, with $\sigma^*(\omega,T) = i\omega\varepsilon_o\varepsilon^*(\omega,T)$, implying $\sigma' = \varepsilon_o\omega\varepsilon''$ and $\sigma'' = \varepsilon_o\omega\varepsilon'(\varepsilon_o =$ vacuum permittivity).

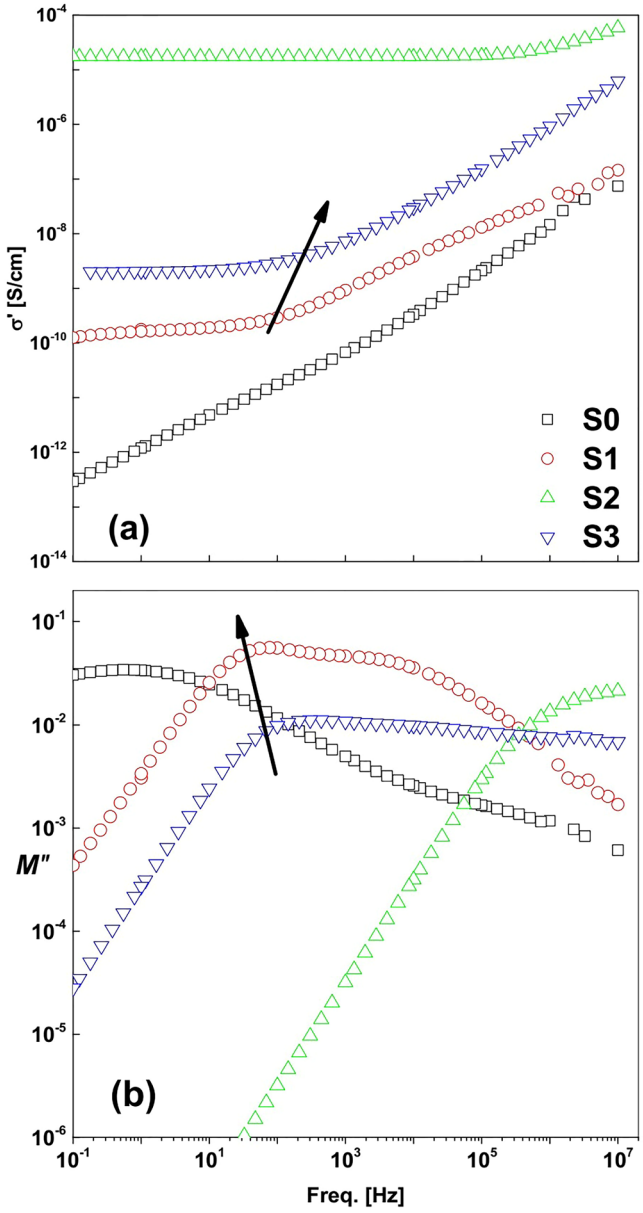


**Figure 9.** Frequency variations of (**a**) σ′ and (**b**) M′′ values plotted at 273 K for four samples $S_0$, $S_1$, $S_2$ and $S_3$ prepared in this investigation.

A gradually increased ε′′ value with increasing temperature describes a thermally induced mobility of charge carriers at these frequencies. This confirms a glassy structure of sample $S_0$. A linear dependence of conductivity on ε′′ explains the results as observed here. A rate of σ′ increase with frequency is slowed down at high frequencies (1 MHz) in a lack of slow dynamic processes. Figure 8 illustrates how σ′ varies over frequencies for a representative sample $S_0$ in two temperature regimes. In the 253 to 293 K regime, σ′ gradually decreases in Fig. 8a on lower frequencies, describing a highly insulating material in the ambient temperature in a freezing like behavior of cold charge carriers at low temperatures[47]. It is worth mentioning that, on warming the sample, the conductivity spreads out at low frequencies as the permittivity described in Fig. 7. The frequency σ′ dependence at higher temperatures (Fig. 8b) follows the well-known Jonscher power-law, as prevails in many conductive glasses and polymeric systems[43–45],

$$\sigma' = \sigma_{dc}[1 + \upsilon/\upsilon_c]^s, \text{ where: } (0 < s \leq 1) \quad (5)$$

At lower frequencies, a less dependent, or even an independent trajectory (plateau) of frequency, builds up. The plateau yields the dc conductivity $\sigma_{dc}$ and characteristic frequency $\nu_c$ in the dispersion of σ′ sets in and turns into a power law at higher frequencies. The $\sigma_{dc}$ is varied by more than two orders in the 373 to 473 K regime.

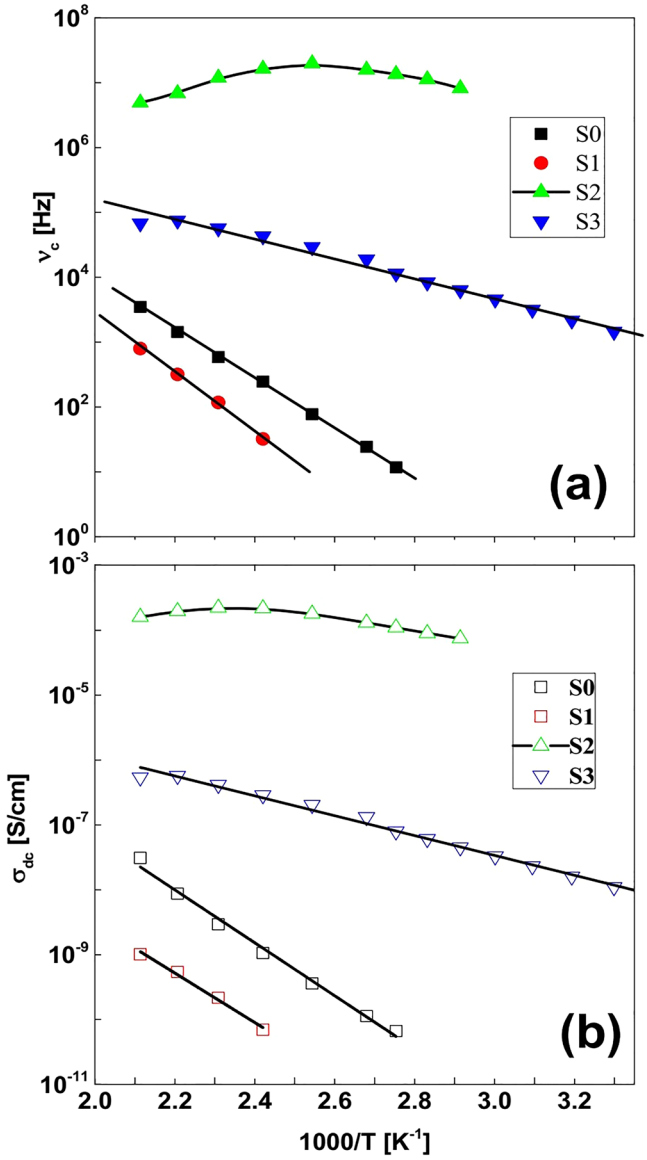


**Figure 10.** Temperature dependence of (**a**) $\nu_c$ and (**b**) $\sigma_{dc}$ values determined by fitting the data in Eq. 5.

Figure 9 depicts $\sigma'$ and electric loss modulus $M''\left(=\frac{\varepsilon''}{(\varepsilon'^2+\varepsilon''^2)}\right)$ as a function of frequency at near 0 K for the four samples. Sample $S_2$, which contains $SrFe_2O_{19}$ with a secondary phase $Sr_3Fe_2(OH)_{12}$, reveals the highest $\sigma'$ value in Fig. 9a at a characteristic frequency (usually called hoping frequency), which is characterized by a maximum peak position in the $M''(\nu)$ plot in Fig. 9b. Samples $S_0$ and $S_1$ peak up $\sigma'$ at higher frequencies and it reflects in a small peak in the $M''$ plots as a result of charges accumulate at potential wells in a kind of interfacial polarization. The charge carriers move short distances accompanied by the relaxation polarization dynamics consistently with what is it is reported earlier[48–50]. Here, a $\sigma_{dc}$ value is related to the characteristic frequency in the maximum peak position in the $M''(\nu)$ plot and not to the peak intensity as marked by the rows. An increasing $\sigma_{dc}$ with increasing characteristic frequency agrees well with the Barton-Nakajima-Namikawa (BNN) relation correlated between dc and ac conductivities, according to $\sigma_{dc} \approx \nu_c$[51–54]. Further, the $M''(\nu,T)$ spectra suggest a remarkably enhanced conductivity on generating mono and multiphase structures over an amorphous sample $S_0$. Thus, sample $S_2$ of three phases has the highest conductivity in the shortest hopping time. Two main parameters of charge transport $\sigma_{dc}$ and $\nu_c$ can be deduced by fitting the data in the Jonscher's universal power law in Eq. 5, with $1 > s > 0.5$. Figure 10 plots so obtained values over $T^{-1}$ for the four samples. Almost all data found to follow an Arrhenius relation:

$$\log(S) = \log(S_\infty) - \frac{\ln 10 E_A}{K_B T} \tag{6}$$

where S could be the dc-conductivity or any other characteristic parameter, $E_A$ is the activation energy and $K_B$ is Boltzmann constant. A value $E_A = 78.1$ kJ/mol found for sample $S_0$ (amorphous) is reduced to be 73.2 kJ/mol for sample $S_1$ (of two phases), or 53.0 kJ/mol for sample $S_3$ of a single phase. In sample $S_2$, which contains three phases, the said plots deviate from the Arrhenius relation, extending a wide peak like behavior. This reflects higher ability of ions to transport in promoted conductivity over other samples. Identical behavior of both parameters in these samples confirms validity of the BNN-relation.

## Experimental work

**Synthesis of samples.** $Sr_4Fe_6O_{13}$ was synthesized using a citrate auto-combustion method. Ferric nitrate and strontium nitrate were mixed in citric acid in the stoichiometric ratio to get a clear solution. Ratio of metal nitrates to citric acid was 1:1. Ammonia solution was added dropwise until the pH became 7. The mixture was stirred at 600 rpm and slowly evaporated at 130 °C to form a gel. Viscosity and color were changed as sol turned into a brown puffy porous dry gel, which then was ignited to burn in a strong auto-combustion process with evolving gases ($CO_2$, $NO_2$, NO, $NH_3$, $CH_4$, etc.). The as-synthesized powder $S_0$ was calcined at 500 °C for 3 h ($S_1$) and at 1100 °C for 3 h ($S_2$), or 10 h ($S_3$), with a heating rate 4 °C/min[55].

**Measurements and analyses.** The structure was examined by an X-ray diffractometer (XRD) of Burker-D8 with Cu-kα radiation of wavelength $\lambda = 1.5418$ Å. Morphology and surface shape of the fine particles was analyzed using a field emission scanning electron microscope (model QUANTA-FEG250, Netherlands) and a transmission electron microscope (TEM) of JEOL-1010. The magnetic measurements were performed using a vibrating sample magnetometer (VSM, LakeShore 7410, USA) with applied fields up to 20 kOe at room temperature. The electrical and dielectric properties were studied of the samples on a long-range of frequency (0.1 Hz to 10 MHz) using a powerful broadband dielectric spectrometer, BDS. It is utilizing a high-resolution Alpha analyzer with an active sample head (Novocontrol GmbH concept 40). All measurements were done isothermally at selected temperatures over 223 to 473 K, which were controlled by a Quatro Novocontrol cryo-system with stability better than ±0.1 K. The samples were sandwiched between two gold-plated brass electrodes of 10 or 20 mm in diameter in parallel plate geometry. The control and data acquisition processes were performed by a WINDETA software[56,57].

## Conclusions

A fine $Sr_4Fe_6O_{13}$ powder was synthesized through a sol-gel auto-combustion method and then annealed at 500 °C for 3 h and at 1100 °C for 3 h, or 10 h in finely tuning its yield of small crystallites. A major phase $Sr_4Fe_6O_{13}$ forms in 1100 °C annealing, with a secondary phase of $SrFe_{12}O_{19}$ and $Sr_3Fe_2(OH)_{12}$. A single phase $Sr_4Fe_6O_{13}$ appears on prolong anneal to 10 h. It shows hard magnetic behavior with $M_s = 12.4$ emu/g, $H_c = 3956.7$ Oe, and $R = 0.512$. It slowly loses $M_s$ but gains $H_c$ on warming over 85 to 305 K in a typical hard magnet. The ac-conductivity follows the well-known Jonscher relation at higher temperatures and it linearly decreases on decreasing frequency at lower temperatures indicating an insulating feature due to freezing of mobility of the charge carriers. The dc-conductivity is related to a characteristic frequency in the Barton-Nakajima-Namikawa relation.

Received: 14 June 2019; Accepted: 18 December 2019;
Published online: 18 March 2020

## References

1. Hoefler, S. F., Trimmel, G. & Rath, T. Progress on lead-free metal halide perovskites for photovoltaic applications: a review. *Monatshefte fur Chemie* **148**, 795–826 (2017).
2. King, G. & Woodward, P. M. Cation ordering in perovskites. *J. Mater. Chem.* **20**, 5785–5796 (2010).
3. Jing, P. *et al*. Width-controlled M-type hexagonal strontium ferrite ($SrFe_{12}O_{19}$) nanoribbons with high saturation magnetization and superior coercivity synthesized by electrospinning. *Sci. Rep* **5**, 15089 (2015).
4. Kanamaru, F., Shimada, M. & Koizumi, M. Crystallographic properties of and mössbauer effect in $Sr_4Fe_6O_{13}$. *J. Phys. Chem. Solids* **33**, 1169–1171 (1972).
5. Fjellvåg, H., Hauback, B. C. & Bredesen, R. Crystal structure of the mixed conductor $Sr_4Fe_4Co_2O_{13}$. *J. Mater. Chem.* **7**, 2415–2419 (1997).
6. Bredesen, R., Norby, T., Bardal, A. & Lynum, V. Phase relations, chemical diffusion and electrical conductivity in pure and doped $Sr_4Fe_6O_{13}$ mixed conductor materials. *Solid State Ionics* **135**, 687–697 (2000).
7. Fossdal, A. *et al*. Phase equilibria and microstructure in $Sr_4Fe_{6-x}CoxO_{13}$ $0 \leq x \leq 4$ mixed conductors. *Solid State Ionics* **143**, 367–377 (2001).
8. Ohkawa, M. *et al*. The structural study of $Sr_4Fe_6O_{13}$ using a Weissenberg technique and synchrotron radiation – unusual ionic radii of five-coordinated Fe3+ ions. *Zeitschrift für Krist. - Cryst. Mater* **212**, 848–854 (1997).
9. MacChesney, J. B., Jetzt, J. J., Potter, J. F., Williams, H. J. & Sherwood, R. C. Electrical and Magnetic Properties of the System $SrFeO_3$-$BiFeO_3$. *J. Am. Ceram. Soc* **49**, 644–647 (1966).
10. Tang, Y. *et al*. Structural chemistry and magnetic properties of the perovskite $Sr_3Fe_2TeO_9$. *J. Solid State Chem.* **242**, 86–95 (2016).
11. Gore, S. K. *et al*. The structural and magnetic properties of dual phase cobalt ferrite. *Sci. Rep* **7**, 2524 (2017).
12. Jalli, J. *et al*. Ferrimagnetic $Sr_{1.5}Ba_{0.5}Zn_2Fe_{12}O_{22}$ (Zn-Y) Single Crystal With Planar Anisotropy. *IEEE Magn. Lett* **2**, 5000104–5000104 (2011).
13. Patrakeev, M. V., Mitberg, E. B., Leonidov, I. A. & Kozhevnikov, V. L. Electrical characterization of the intergrowth ferrite $Sr_4Fe_6O_{13+\delta}$. *Solid State Ionics* **139**, 325–330 (2001).
14. Pardo, J. A. *et al*. Thickness-dependent transport properties of $Sr_4Fe_6O_{13}$ epitaxial thin films. *Solid State Ionics* **177**, 423–428 (2006).
15. Ma, B. *et al*. Structure and Property Relationships in Mixed-Conducting $Sr_4(Fe_{1-x}Cox)_6O_{13\pm\delta}$ Materials. *J. Solid State Chem.* **141**, 576–586 (1998).
16. Yoshiasa, A., Ueno, K., Kanamaru, F. & Horiuchi, H. Structure of $Sr_4Fe_6O_{13}$, a new perovskite-derivative in the $Sr_4Fe_6O_{13}$ system. *Mater. Res. Bull.* **21**, 175–181 (1986).
17. Guggilla, S. & Manthiram, A. Crystal Chemical Characterization of the Mixed Conductor $Sr(Fe, Co)_{[sub\ 1.5]}O_{[sub\ y]}$ Exhibiting Unusually High Oxygen Permeability. *J. Electrochem. Soc.* **144**, L120 (1997).

18. Waerenborgh, J. C., Avdeev, M., Patrakeev, M. V., Kharton, V. V. & Frade, J. R. Redox behaviour of $Sr_4Fe_6O_{13\pm\delta}$ by Mössbauer spectroscopy and neutron diffraction. *Mater. Lett.* **57**, 3245–3250 (2003).
19. Orlovskaya, N. & Browning, N. D. *Mixed ionic electronic conducting perovskites for advanced energy systems*. (Kluwer Academic Publishers, 2004).
20. Bouwmeester, H. J. M. Chapter 10 Dense ceramic membranes for oxygen separation. In *Membrane Science and Technology* **4**, 435–528 (Elsevier, 1996).
21. Badwal, S. P. S. & Ciacchi, F. T. Ceramic membrane technologies for oxygen separation. *Adv. Mater.* **13**, 993–996 (2001).
22. Hashim, S. S., Mohamed, A. R. & Bhatia, S. Oxygen separation from air using ceramic-based membrane technology for sustainable fuel production and power generation. *Renew. Sustain. Energy Rev.* **15**, 1284–1293 (2011).
23. Kilner, J. A. Fast oxygen transport in acceptor doped oxides. *Solid State Ionics* **129**, 13–23 (2000).
24. Fisher, C. A. J. & Islam, M. S. Mixed ionic/electronic conductors $Sr_2Fe_2O_5$ and $Sr_4Fe_6O_{13}$: atomic-scale studies of defects and ion migration. *J. Mater. Chem.* **15**, 3200 (2005).
25. Jean, M., Nachbaur, V., Bran, J. & Le Breton, J. M. Synthesis and characterization of $SrFe_{12}O_{19}$ powder obtained by hydrothermal process. *J. Alloys Compd.* **496**, 306–312 (2010).
26. Patterson, A. L. The scherrer formula for X-ray particle size determination. *Phys. Rev* **56**, 978–982 (1939).
27. Zsigmondy, R. & Scherrer, P. Bestimmung der inneren Struktur und der Größe von Kolloidteilchen mittels Röntgenstrahlen. *in Kolloidchemie Ein Lehrbuch* **1918**, 387–409 (1912).
28. Shintani, T. & Murata, Y. Evaluation of the dislocation density and dislocation character in cold rolled Type 304 steel determined by profile analysis of X-ray diffraction. *Acta Mater.* **59**, 4314–4322 (2011).
29. Ram, S. Crystallisation of $BaFe_{12}O_{19}$ hexagonal ferrite with an aid of $B_2O_3$ and the effects on microstructure and magnetic properties useful for permanent magnets and magnetic recording devices. *J. Magn. Magn. Mater.* **82**, 129–150 (1989).
30. Smit, J. & Wijn, H. P. J. *Ferrites: physical properties of ferrimagnetic oxides inrelation to their technical applications*. (Wiley, 1959).
31. Pullar, R. C. Hexagonal ferrites: A review of the synthesis, properties and applications of hexaferrite ceramics. *Progress in Materials Science* **57**, 1191–1334 (2012).
32. Zhang, H., Wang, T., Chen, X. & Zhu, W. Controllable hydrothermal synthesis of star-shaped $Sr_3Fe_2(OH)_{12}$ assemblies and their thermal decomposition and magnetic properties. *Particuology* **24**, 210–215 (2016).
33. Lin, C. R., Chu, Y. M. & Wang, S. C. Magnetic properties of magnetite nanoparticles prepared by mechanochemical reaction. *Mater. Lett.* **60**, 447–450 (2006).
34. Chen, D. H. & Chen, Y. Y. Synthesis of barium ferrite ultrafine particles by coprecipitation in the presence of polyacrylic acid. *J. Colloid Interface Sci.* **235**, 9–14 (2001).
35. Franco, A., Pessoni, H. V. S. & Machado, F. L. A. Spin-wave stiffness parameter in ferrimagnetic systems: Nanoparticulate powders of (Mg, Zn) $Fe_2O_4$ mixed ferrites. *J. Appl. Phys.* **118**, 173904 (2015).
36. Vázquez-Vázquez, C., López-Quintela, M. A., Buján-Núñez, M. C. & Rivas, J. Finite size and surface effects on the magnetic properties of cobalt ferrite nanoparticles. *J. Nanoparticle Res* **13**, 1663–1676 (2011).
37. Mandal, K., Mitra, S. & Kumar, P. A. Deviation from Bloch T3/2 law in ferrite nanoparticles. *Europhys. Lett.* **75**, 618–623 (2006).
38. Nguyet, D. T. T., Duong, N. P., Hung, L. T., Hien, T. D. & Satoh, T. Crystallization and magnetic behavior of nanosized nickel ferrite prepared by citrate precursor method. *J. Alloys Compd.* **509**, 6621–6625 (2011).
39. Cojocaru, S. Temperature dependence of magnetization of a nanosize Heisenberg ferromagnet. *Optoelectron. Adv. Mater. Rapid Commun* **5**, 1196–1201 (2011).
40. Nagai, N., Sugita, N. & Maekawa, M. Formation of hexagonal, platelike Ba-ferrite particles with low temperature dependence of coercivity. *J. Magn. Magn. Mater.* **120**, 33–36 (1993).
41. Chagas, E. F. *et al*. Thermal effect on magnetic parameters of high-coercivity cobalt ferrite. *J. Appl. Phys.* **116**, 033901 (2014).
42. Nihon Butsuri Gakkai. & Ōyō Butsuri Gakkai. Temperature Dependence of Coercivity Behavior in Fe Films on Fractal Rough Ceramics Surfaces. *Japanese J. Appl. Phys. JJAP.* **52**, 01AC13-1–4 (2013).
43. Sharma, S. K., Rajeswari, P. V., Tiwari, B. & Ram, S. Hydrothermal synthesis of LiMnPO4-C(sp2) hybrids, conductive channels, and enhanced dielectric permittivity: a modulated ionic conductor. *Ionics (Kiel).* **23**, 43–53 (2017).
44. Tiwari, B., Ram, S. & Banerji, P. Biogenic Synthesis of Tunable Core-Shell C-$CaIn_2O_4$, Interface Bonding, Conductive Network Channels, and Tailored Dielectric Properties. *ACS Sustain. Chem. Eng.* **6**, 16298–16307 (2018).
45. Elliott, S. R. Temperature dependence of a.c. conductivity of chalcogenide glasses. *Philos. Mag. B* **37**, 553–560 (1978).
46. Azab, A. A. *et al*. Structural and dielectric properties of prepared PbS and PbTe nanomaterials. *J. Semicond.* **39**, 123006 (2018).
47. Abd El-Aziz, M. E., Youssef, A. M., Kamel, S. & Turky, G. Conducting hydrogel based on chitosan, polypyrrole and magnetite nanoparticles: a broadband dielectric spectroscopy study. *Polym. Bull.* **76**, 3175–3194 (2019).
48. Dhankhar, S. *et al*. Electrical conductivity and modulus formulation in zinc modified bismuth boro-tellurite glasses. *Indian J. Phys.* **90**, 1033–1040 (2016).
49. Moussa, M. A. *et al*. Dielectric investigations and charge transport in PS-PAni composites with ionic and nonionic surfactants. *J. Phys. Chem. Solids* **133**, 163–170 (2019).
50. Biswas, D. *et al*. Conductivity spectra of silver-phosphate glass nanocomposites: Frequency and temperature dependency. *J. Non. Cryst. Solids* **495**, 47–53 (2018).
51. Turky, G., Sangoro, J. R., Rehim, M. A. & Kremer, F. Secondary relaxations and electrical conductivity in hyperbranched polyester amides. *J. Polym. Sci. Part B Polym. Phys* **48**, 1651–1657 (2010).
52. Macdonald, J. R. Universality, the Barton Nakajima Namikawa relation, and scaling for dispersive ionic materials. *Phys. Rev. B - Condens. Matter Mater. Phys.* **71**, (2005).
53. Sangoro, J. R. *et al*. Charge Transport and Dipolar Relaxations in Hyperbranched Polyamide Amines. *Macromolecules* **42**, 1648–1651 (2009).
54. Turky, G., Shaaban, S. S. & Schöenhals, A. Broadband dielectric spectroscopy on the molecular dynamics in different generations of hyperbranched polyester. *J. Appl. Polym. Sci.* **113**, 2477–2484 (2009).
55. Azab, A. A., El-Dek, S. I. & Solyman, S. Unsual features of ferromagnetic/antiferromagnetic nanocomposites. *J. Alloys Compd.* **656** (2016).
56. Broadband Dielectric Spectroscopy, https://doi.org/10.1007/978-3-642-56120-7 (Springer Berlin Heidelberg, 2003).
57. Moussa, M. A. *et al*. Relaxation dynamic and electrical mobility for poly(methyl methacrylate)-polyaniline composites. *J. Appl. Polym. Sci.* **134**, 45415 (2017).


## Author contributions

A.A. Azab, Sample preparation, data analysis, preparation of manuscript, and discussion of the results with equal contributions. A. M. Mansour, Data analysis and calculation of XRD and preparation the manuscript and discussion the results with equal contributions. G. Turky, Discussion of the results with equal contributions, and revision of the manuscript in the final version.

## Competing interests

The authors declare no competing interests.

## Additional information

**Correspondence** and requests for materials should be addressed to A.A.A.

**Reprints and permissions information** is available at www.nature.com/reprints.

**Publisher's note** Springer Nature remains neutral with regard to jurisdictional claims in published maps and institutional affiliations.